Accepted Article Preview: Published ahead of advance online publication

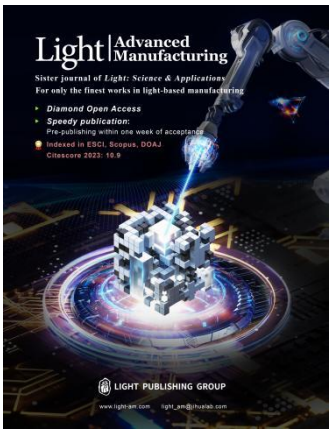

Single-Step Holographic Grayscale Lithography of Fabry-Perot Filter Arrays

Oliver J. Burton, Marco Astarita, Ayan Rakshit, Peter J. Christopher, Calum Williams, Jack Alexander-Webber, Tim Wilkinson, Hannah Joyce

Cite this article as: Oliver J. Burton, Marco Astarita, Ayan Rakshit, Peter J. Christopher, Calum Williams, Jack Alexander-Webber, Tim Wilkinson, Hannah Joyce. Single-Step Holographic Grayscale Lithography of Fabry-Perot Filter Arrays. *Light: Advanced Manufacturing* accepted article preview 24 April, 2026; doi: 10.37188/lam.2026.076

Received 13 November 2025; Revised 22 April 2026; Accepted 24 April 2026; Accepted article preview online 24 April 2026

Single-Step Holographic Grayscale Lithography of Fabry–Perot Filter Arrays

Oliver J. Burton[1] † *, Marco Astarita[2] *, Ayan Rakshit[1], Peter J. Christopher[3], Calum Williams[4], Jack Alexander-Webber[1], Tim Wilkinson[1], and Hannah Joyce[1]

[1]*Department of Engineering, University of Cambridge, 9 JJ Thomson Avenue, Cambridge, CB3 0FA, United Kingdom.*
[2]*Politecnico di Milano, Piazza L. da Vinci 32, 20133 Milano, Italy*
[3]*Department of Engineering, University Park, Nottingham NG7 2RD, United Kingdom.*
[4]*Department of Physics, University of Exeter, Exeter, EX4 4QL, United Kingdom*
*These authors contributed equally to this work.
†Correspondence to: Oliver J. Burton: ob303@cam.ac.uk

Abstract

Multispectral filter arrays underpin compact spectral imaging but are typically fabricated through complex multistep photolithography. Herein, we demonstrate a single-step holographic grayscale lithography method that uses a spatial light modulator to directly write Fabry–Perot filter arrays. A phase-retrieval algorithm is used to compute holograms that project grayscale intensity patterns onto a photoresist, enabling cavity thicknesses ranging from 600 to 1300 nm across a single exposure. IN this study, transmission spectra were modelled using transfer-matrix simulations with Monte Carlo averaging to capture thickness variations, and experimental spectra were fitted via Tikhonov-regularized inversion. Good agreement was observed between the theory and experiment ($R^2 \approx 0.95$). We demonstrated that speckle-like noise, which is typically detrimental to projection systems, can be exploited as a design parameter to broaden Fabry–Perot resonances in a controllable manner. Additionally, the method can achieve lateral resolutions down to 1-2.5 μm depending on the resolution criteria, thus representing the highest resolution reported for holographic projection lithography and comparable to many commercial direct-write techniques. This approach consolidates multiple fabrication steps, offering a scalable and tuneable route toward integrated multispectral filter arrays compatible with CMOS imaging technology.

Keywords: Holography, Spectral Filters, Fabrication, Grayscale Lithography.

Introduction

The on-chip fabrication of optical filters for use in spectral imaging has become prominent in the research on multi-spectral imaging. Filter arrays spatially modulate the allowed frequencies of light that can reach each pixel, similar to a Bayer filter for red, blue, and green in traditional colour cameras[1]. These multispectral filter arrays retain the integration advantages of Bayer filters while enabling targeted spectral resolution (or those of even more complex spectral structures[2, 3]). Their applications include precision agriculture, environmental monitoring, and medical diagnostics, where rich spectral data can provide detailed chemical and structural information[4, 5, 6, 7, 8].

Existing methods for patterned filter arrays, including multilayer dielectric stacks[9], plasmonic filters[10], and metasurfaces[11], typically require complex, multistep photolithography with physical masks[2] or slow direct-write methods, such as electron beam lithography[9, 12, 13] occasionally combined with numerous material deposition stages. Fabry-Perot filters, specifically metal-insulator-metal structures[14], are simpler to fabricate and design, which has facilitated their adoption in both industry and academia[15, 2, 16]. Although many different methodologies for producing or selecting these filters exist[17, 1, 18, 12], they still rely on multistep photolithography using masks[14, 19, 20] or slower scanning-based approaches, such as electron beam lithography[14], to pattern each of

the many individual filters.

The most common methodology uses many separate photolithography stages, with multiple depositions and exposures to build the requisite stack[14, 19, 20]. Grayscale lithography, in which the intensity of light on the photoresist is nonbinary, can be used to fabricate these multispectral filter arrays; however, it suffers from several inherent challenges. Mask-based processes require intricate and expensive masks, whereas digital micromirror device (DMD)-based techniques are constrained to discrete intensity levels because of their binary nature. Furthermore, the pixel size and pitch of DMDs limit their achievable resolution and pattern complexity[21] when predicting the precise alignment of DMD pixels to areas or features of interest.

Recently, computer-generated holography (CGH) has become increasingly common in applications related to novel display technologies, partly because of the availability of higher-quality spatial light modulators (SLMs). In typical systems that use a phase-modulating liquid crystal-on-silicon (LCOS) SLM, an iterative phase-retrieval algorithm computes an optimal phase-only hologram, a two-dimensional phase mask, for a given target intensity pattern. When this phase mask is displayed on the SLM, it spatially modulates the phase of the incident expanded coherent beam. A subsequent Fourier-transforming lens then reconstructs the target intensity pattern in its back focal plane, which is commonly referred to as the replay field. This Fourier relationship between the SLM and replay field is key; it dictates that the image resolution and feature shapes are not directly constrained by the SLM's pixel structure, thus sidestepping many of the disadvantages of a DMD based projection. In addition, the reconstructed intensity is inherently continuous, enabling true grayscale levels for arbitrary shapes. Holograms have previously been used in binary maskless lithography, with previous methods in this field enabling the exposure of binary patterns on photoresists[22, 23, 24]. A core advantage of holographic optics is its ability to concatenate desired optical effects within the hologram itself, including the potential for aberration correction and image shifting for alignment.

Herein, we present a holographic lithography apparatus using an LCOS-SLM that natively supports grayscale light projection on arbitrary substrates and demonstrate the single-step fabrication of Fabry–Perot filter arrays, as illustrated in Fig. 1. We show that these filters have definable cavity thicknesses within a projected image, and we introduce a novel tunability mechanism that harnesses speckle-like noise as a design parameter to control the filter linewidth. We also demonstrate that our methodology can achieve resolutions as low as 1-2.5 µm.

Experimental details

Optical set-up

Our holographic photolithography setup is shown in Fig.2. The exposure source was a 405 nm diode laser (Coherent OBIS LX SF). Its intensity could be optimised according to the required exposure dose using a variable attenuator composed of a rotatable half-wave plate (HWP) and polarising beam splitter (PBS). The beam was then expanded and cleaned using a spatial filter consisting of a telescope (L_1, f=25.4 mm; L_2, f=400 mm) with a 20 μm pinhole (PH) placed in the focal plane. An iris (I) was used to set the beam size to match the dimensions of the SLM's active area.

The prepared beam illuminated a phase-only SLM (Santec SLM-250), which encodes a computer-generated hologram onto the wavefront. The modulated light then enters a 4f relay system (L_3, f=150 mm; L_4, f=125 mm), which serves two purposes: it provides an accessible Fourier plane for filtering the zeroth diffraction order with a 500 μm beam block ($\sim PH$) and relays the SLM plane, forming a demagnified image of the phase pattern on the back focal plane of the final objective. The microscope objective (OBJ: RMS4X, 0.10 NA) acted as a Fourier-transforming lens, reconstructing the desired grayscale intensity pattern in its focal plane where the photoresist-coated sample was placed.

An imaging path was integrated into the setup for precise sample positioning and inspection. A beamsplitter (BS) directed the light scattered by the sample through L_4 to a CMOS camera (Alvium 1800 U-040m), offering a magnified view (M = 2.78). This path could be used with either a 405 nm laser to precisely align the sample surface with the objective's focal plane, ensuring that it is in focus for holographic projection, or with white-light illumination for non-invasive in-situ observation of the fabricated structures.

Hologram generation

The phase holograms displayed on the SLM were computed using a modified iterative algorithm based on the Gerchberg-Saxton (GS)[25] method (Fig. 3). We implemented several variations, primarily from the study of Chen et al. [26], to optimise the uniformity and linearity of the intensity response. This ensured that the target grayscale values were reproduced in the replay field, which is a critical requirement for precise dose control in photolithography.

The standard GS process begins with a target intensity pattern, I_{input}, initialising the Fourier plane field $U_F = \sqrt{I_{input}}$ with a random phase ϕ_0. An inverse Fourier transform yields the SLM-plane field, where the amplitude is constrained to match the input beam profile while the phase is retained. A forward transform then returns to the Fourier plane, where the amplitude is reset to the target while the new phase is saved. This loop is repeated for a set number of iterations.

The key variations we implemented from [26] included three main features: a weighted constraint strategy, energy conservation, and target oversampling. The oversampling step, which is required to correctly sample the intensity fluctuations, involves resampling an $M \times M$ target to a $2M \times 2M$ grid via sinc interpolation. The weighted

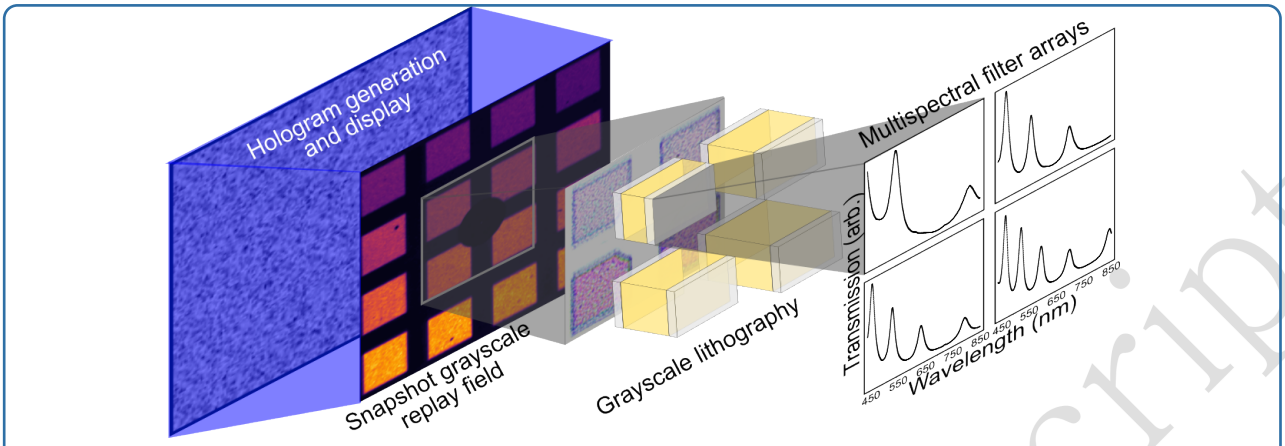

Fig. 1. Schematic illustration of the holographic grayscale lithographic patterning of a multispectral filter array, with an example of measured transmission spectra shown on the right-hand side

constraint strategy then partitions this $2M \times 2M$ Fourier plane into a 'signal region' (SR) and 'noise region' ($\notin SR$). The iterative amplitude constraint is applied asymmetrically: the amplitude in the SR is forced to match the target $\sqrt{I_{input}}$, whereas the amplitude in the noise region is allowed to float freely (*i.e.* it is not constrained to zero). This 'amplitude freedom', combined with the enforcement of energy conservation at each iteration, effectively suppresses artifacts and improves signal uniformity.

Finally, to counteract the intensity roll-off caused by the SLM's pixelated structure (*i.e.* the sinc envelope), we pre-correct the target amplitude by dividing it by $sinc^{\alpha}(x)sinc^{\alpha}(y)$. Although the theoretical value is $\alpha = 2$, we found that the empirical tuning of this parameter (typically near 2) yields the best corrective results.

Filter Fabrication and Simulation

We used holographic grayscale lithography to fabricate Fabry–Perot filters owing to their prominent development in spectral camera research [16, 15, 9]. The filter structure consisted of a photoresist cavity defined between two semi-reflective silver layers. The fabrication began with the electron-beam evaporation of a 26 nm Ag layer onto a quartz substrate, followed by a 2 nm protective SiO_2 capping layer to reduce the propensity to tarnish during the remainder of the lithography procedure. A metal thickness of 26 nm was selected to balance the peak widths to ensure resolvability at broader distributions of polymer thicknesses while not significantly reducing transmission owing to absorption. An AZ5214E photoresist was spin-coated at 4000 rpm to serve as the photoactive layer, yielding an initial thickness of approximately 1500 nm. Each exposure produced a 4×4 array of Fabry–Perot cavities (200 µm side length). Each hologram encoded 16 distinct grayscale levels designed to produce cavities with systematically varying thicknesses. To investigate the dose response and time multiplexing, we fabricated 14 separate 4×4 arrays with exposure times between 20 and 150 s, corresponding to a varying number of hologram refreshes at a fixed frame rate of 5 Hz. We estimated that given the errors at a power calibration (from the Thorlabs PM16-120 power meter) of $\approx 3\%$, the laser power stability of $\approx 2\%$ (from the Coherent OBIS 405 nm specifications), and the timing uncertainty of the exposure sequence $\approx 0.33\% - 2.5\%$, the error in the dose is of the order of approximately $\approx 4.4\%$ Following exposure, the samples were developed using an AZ 726 MIF developer for 60 s and coated with a second 26 nm silver layer to complete the Fabry–Perot stack (examples of scanning electron micrographs are shown in SI Fig. 5). These filters were constructed and measured without any final encapsulation layer. However, owing to the varying tarnishing mechanisms of silver, an inert capping layer to prevent exposure to the elements is recommended to preserve the filter function over time in commercial applications.

To model the transmission spectra, we used the transfer-matrix method (TMM), which is a widely established technique for stratified media [27, 28] combined with Monte Carlo sampling (see SI S2). In this approach, the photoresist thickness is treated as a Gaussian-distributed variable with a standard deviation of σ_p to represent spatial fluctuations and speckle-related variations. For each nominal thickness, 5000 random samples were drawn, and the resulting transmission spectra were averaged to yield broadened peak profiles. Two illustrative cases are presented in Fig. 4, which compares $\sigma_p = 0$ nm and $\sigma_p = 50$ nm while highlighting the peak broadening due to thickness variations. Silver optical constants were obtained from the study of Johnson and Christy[29], and the photoresist refractive index was modelled using a three-term Cauchy relationship fitted to the ellipsometry data of the photoresist shown in SI Fig. S2. Note that, in this paper, we consider only the transparent spectral range of the polymer used (450–850 nm), which had

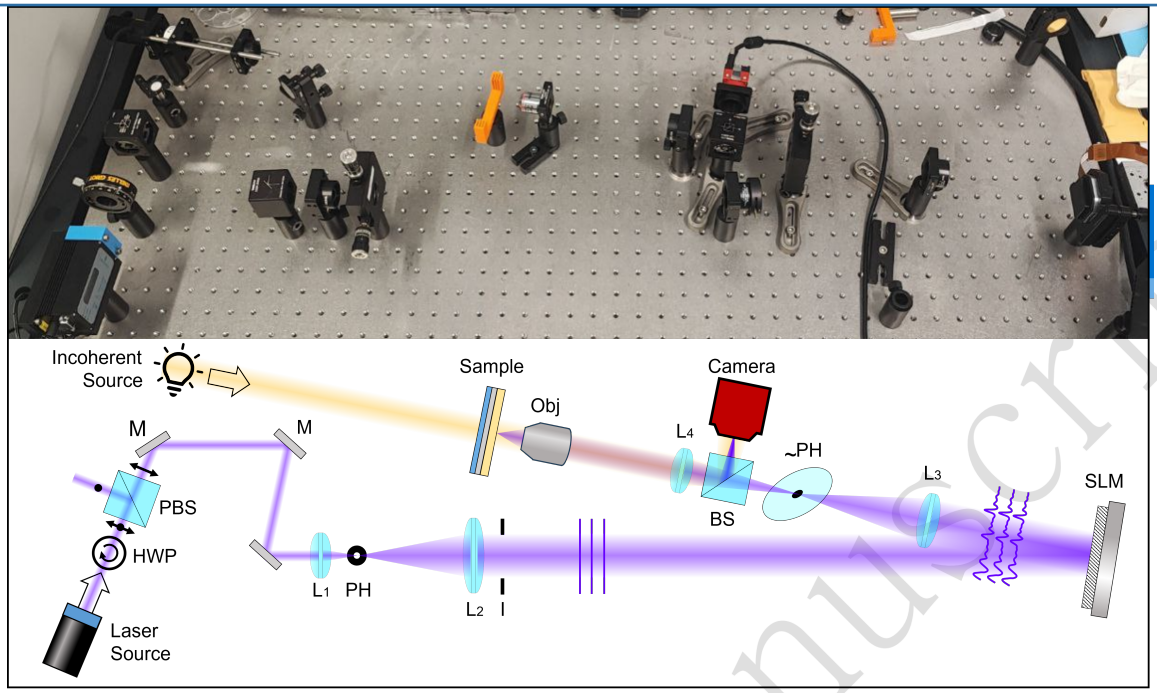

Fig. 2. Photograph and schematic explanation of the optical set-up used in this study. Briefly: the laser is appropriately polarized, aligned and spatially filtered before incidence on the SLM. The light is then taken through a 4f system to remove the 0th order before being passed through a microscope objective and focused onto the photoresist. A second incoherent light source is used to image and align the sample to the replay field.

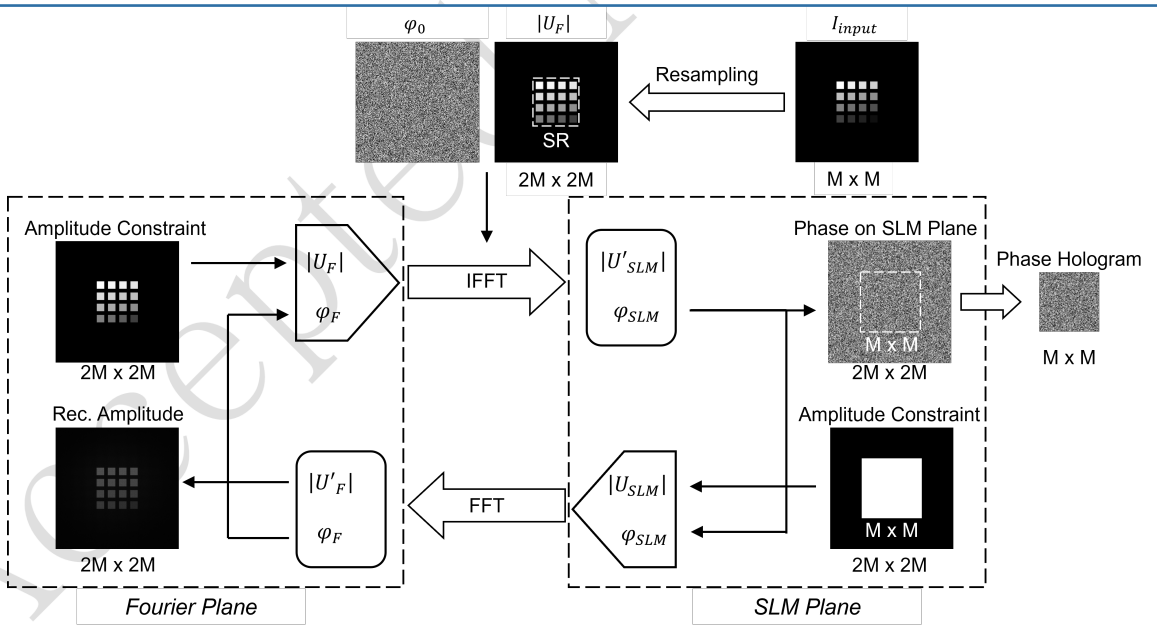

Fig. 3. Schematic of the CGH GS-based algorithm: The M by M target amplitude is resampled to 2M by 2M and initialized with a random phase. An iterative loop, consisting of an IFFT to the SLM plane (where amplitude is constrained to uniform in the central M by M region and zero outside), is then performed followed by an FFT back to the target plane (where amplitude is constrained to the target within the 'signal region' while being left unconstrained in the surrounding 'noise region'). The sequence is repeated until convergence, and the final CGH is the phase resulting in the central M by M SLM region.

negligible extinction; for wavelengths outside this range, a sufficient model of the extinction coefficient would also be required.

We measured these experimental spectra using an OceanOptics SR4 visible spectrometer (spot diameter $\approx 100\,\mu\text{m}$; see SI Figure S5) with a ThorLabs tungsten-halogen light source (SLS201L). As the experimental spectra included broadening from local thickness variations, we used a Tikhonov-regularized inverse fitting scheme to extract the underlying thickness distribution[30]. The peaks in the measured spectra were identified through a prominence analysis, and the corresponding thicknesses were estimated using the Fabry–Perot resonance condition, $2Re\{n\}d = m\lambda + \phi$, where n is the refractive index, d is the cavity thickness, m is the mode order, ϕ is the phase shift, and λ is the wavelength. A basis set of 200 simulated spectra was generated around this thickness estimate, spanning $\pm 0.25d$. Tikhonov regularization was used to provide an estimate of the underlying thickness distribution, which was approximately Gaussian. We then fit this thickness distribution with a Gaussian distribution to extract the mean thickness and standard deviation. This fitting procedure achieved a mean coefficient of determination of $R^2 = 0.953 \pm 0.003$, thus validating the approach.

Results and Discussion

Filters with cavity thicknesses starting from 600–1300 nm were fabricated by varying the cumulative dose and multiplexing holograms. The dose was calculated by taking the total power of the replay field (as measured using a Thorlabs power meter; PM100) and distributing the fluence to each filter by imaging the replay field using a camera. From a pragmatic perspective, we note that this range of cavity thicknesses was a function of the resist thickness and dosage used in this study. Different cavity thickness ranges can be achieved by varying the dose and photoresist thickness or by using photoresists with varying relationships between exposure and development. Fig. 5 shows the strong correlation between dose and fitted mean thickness, showing that they broadly agreed with expected dose-development trends from the literature for other photoresists[14, 31]. This demonstrated that although the total time of exposure varied significantly (by almost an order of magnitude) between the sets of 16 filters, the total dose was the largest contributing parameter that dictated the final thickness of the photoresist. Despite this strong relationship, a noticeable variation was observed in the doses for a given development or end thickness, with higher exposure times requiring a larger dose to achieve the same post-development thickness. This slight variation could be attributed to several potential effects, such as a slight nonlinear response of the CMOS image sensor used for dose allocation to the true light intensity or a dependence on exposure time as well as the dose for the photoresist development rate. This shows that careful calibration and understanding of these interplaying

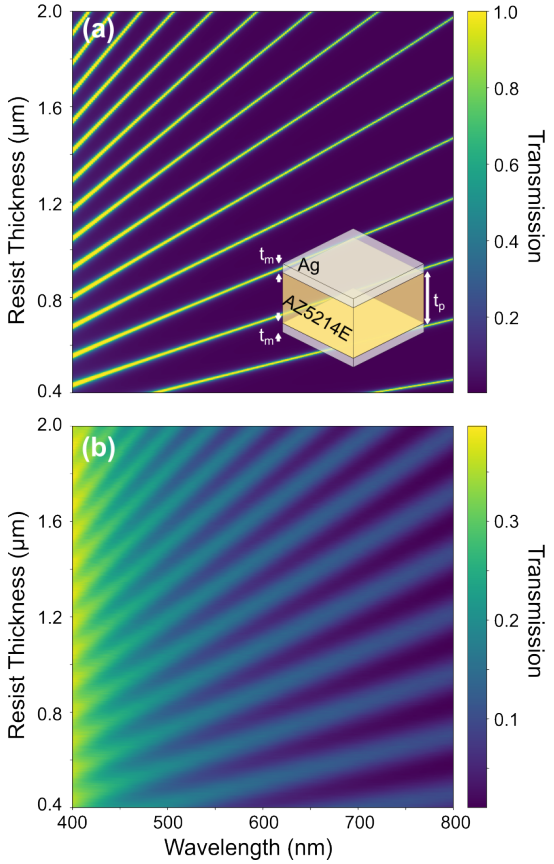

Fig. 4. Heat maps showing the results of multiple TMM Monte Carlo simulations of the Fabry-Perot filters for a range of mean thicknesses. The results for different Gaussian distributions are shown: (a) $\sigma_p = 0$ and (b) $\sigma_p = 50$ nm for a range of resist thicknesses.

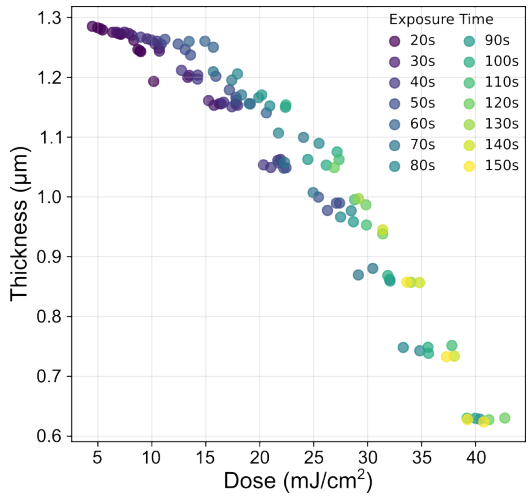

Fig. 5. Plot of the mean photoresist (*i.e.* cavity) thickness as a function the net dose received by the photoresist, with the point colour indicating exposure time.

parameters are required for the precise control demanded by commercial realisation. Regardless, the wide tunability of photoresist exposure and development demonstrates that holographic grey-scale lithography can produce cavities spanning a thickness range of approximately $0.7\,\mu\mathrm{m}$ in a single exposure without recourse to multistep processes involving 16 different individual exposures and masks or mask realignments.

Fig. 6 shows a representative microscope image of a 4×4 array, together with example spectra and fitted results. The transmission spectra show Fabry–Perot resonances whose peak wavelengths shifted predictably with the cavity thickness. Within a given 4×4 array, the reproducibility was high, with filter elements of similar doses producing closely matched spectral features. Across the 14 stepped arrays, the systematic red shift with increased total dose demonstrated a controlled scaling of thickness by controlling the exposure time, laser power, and intensity determined by the target replay field.

Spectral linewidths in the samples described in this study were found to vary between approximately $10\,\mathrm{nm}$ and $30\,\mathrm{nm}$, depending on wavelength and order, corresponding to fitted physical thickness spreads between $19\,\mathrm{nm}$ and $50\,\mathrm{nm}$. These values were consistent with the TMM Monte Carlo simulations, which predicted a similar broadening of the Fabry–Perot peaks under (Gaussian) fluctuations in thickness. A typical $R^2 \approx 0.95$ indicated good agreement between the experiment and fitted simulation. A comparison between the simulated cases of $\sigma_p = 0$ and $\sigma_p = 50\,\mathrm{nm}$ in Fig. 4 shows that varying the distributions of thicknesses

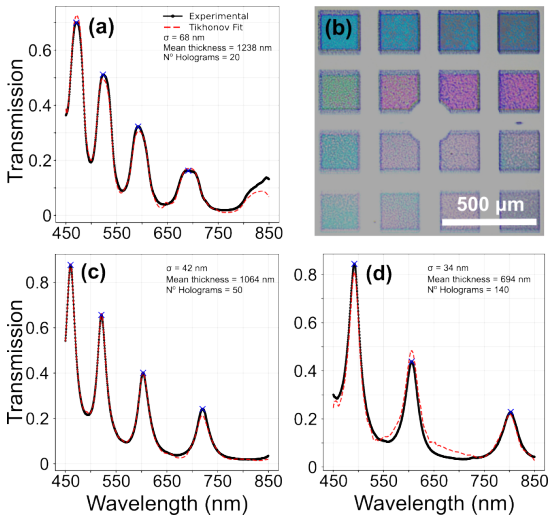

Fig. 6. (a) Optical image showing an example holographically patterned filter array, consisting of quartz, $26\,\mathrm{nm}$ Ag, the developed photoresist, and $26\,\mathrm{nm}$ Ag. (b–d) Examples of measured transmission spectra showing the different spectral characteristics of filters with different thicknesses and the model fits, where σ corresponds to the fitted width of the Gaussian distribution of thicknesses, the mean thickness corresponds to the fitted mean thickness of the photoresist, and the N^o holograms correspond to the number of holograms used to create that specific filter.

present in a filter, modulated by speckle and/or speckle-like noise, can function as an intrinsic broadening mechanism for the transmission peaks.

A key advantage of holographic lithography is the ability to create multiple filter thicknesses during a single exposure. In contrast, conventional methods would require 16 separate exposures to fabricate a 4×4 array of distinct Fabry–Perot cavities. Therefore, holographic grayscale lithography enables a significant reduction in process complexity. The presence of speckle-like noise, typically a limitation in display and projection applications, is repurposed as a design parameter: By adjusting the number of holograms and exposure time, we can tune the effective broadening of the transmission peaks. This represents a novel strategy for linewidth control without altering mirror reflectivity, which is the conventional approach in Fabry–Perot design [32, 33] and has yet to be demonstrably varied in multispectral filter arrays owing to the complexity of depositing distinct thicknesses of adjacent metals.

Interestingly, we note that the additional time multiplexing, defined by the total number of different holograms shown, used in this study can initially appear to increase the degree of roughness of the filters rather than decrease it. Fig. S3 shows the general trend in peak width for samples of different exposure times; while a broad increase in peak width was observed with exposure time, when the data were sectioned into regions of similar thickness (through k-means clustering) and plotted against the number of holograms, that trend was broadly reversed. Thus, given a dose leading to a particular thickness, increasing the number of holograms leads to a decrease in the roughness of the photoresist and narrows the transmission peak widths. A convenient method is to break down the trends into two competing effects: the first is the effect of prolonged exposure in the context of the nonlinear response of photoresists to cumulative doses[31, 34, 35], where high-intensity and persistent speckles or speckle-like noise reaches saturation earlier than low-intensity regions, thereby amplifying local thickness variations with increasing exposure. Second, the opposing effect is the speckle averaging from time multiplexing, which is designed to reduce these nonuniformities. By displaying a large number of independently generated holograms, high-frequency spatial noise is averaged out, creating a smoother and more uniform exposure profile that decreases the final surface roughness.

No consistently visible persistent noise pattern was apparent in the different exposures, indicating that the noise due to the holograms was unlikely to be correlated, which is generally expected because of the randomisation of the phase during hologram generation. However, the increase in roughness with additional exposure time might indicate some noise independent of the randomisation of the initial phase of the holograms when generated, which may be a factor of the optical system beyond the LCOS-SLM used to modulate the phase. Alternatively, it could be a result of the development process, whereby the roughness distribution acts to increase as a ratio to the thickness (*i.e.* the thinner the developed polymer, the larger the rough features compared with the mean thickness). Consequently, prolonged exposure can enhance roughness despite time-multiplexing, which only serves to decrease roughness when the exposure dose is approximately the same. This highlights the importance of carefully balancing exposure time and multiplexing strategy for optimal filter quality. This trade-off effectively introduces an extra degree of freedom into the process. Our results show that the same total dose can be delivered with a low intensity over a long time or with a high intensity over a short time. This choice enables the tuneable control of the final surface roughness, which directly affects and controls the linewidths of the spectral peaks. The spatial scale of the noise (and, therefore, the resultant variations in thickness) is also a function of the focal length/magnification of the Fourier lens used to create the replay field. Thus, at higher magnifications, the noise has a higher spatial frequency, as it effectively 'shrinks' with the replay field. Thus, the magnification used for lithography also controls the characteristics of the peak-broadening effect described above.

The primary limitations of the current methodology are the exposure time and the presence of hologram-independent speckles (*i.e.* noise that persists across randomly generated holograms). However, this is primarily a technological constraint specific to the SLM used in this study. The development of higher-frame-rate SLMs is already leading to, and will, in the future, enable much shorter exposure times and, with additional optimisation of the optical system, include the implementation of commonly used speckle reduction techniques[36, 37].

By patterning Siemens stars using holographic lithography, we can approximate the resolution limit of the technique, as detailed in the Supplementary Information (see SI Fig. S4). This methodology, similar to an optical MTF10 measurement of an imaging system's resolution, reported lithographic feature sizes down to approximately $1\,\mu\mathrm{m}$; however, this type of measurement effectively averages out roughness/perturbations to the resist due to speckle-like noise. Thus, by eye, we also measured the smallest feature present on all spokes to be approximately less than $2.5\,\mu\mathrm{m}$, giving a more conservative estimate. This is comparable to the results reported for holographic projection lithography for binary (*i.e.* non-grayscale) patterns[22, 23, 24], approaching the classical diffraction limit of a system of approximately $0.5\,\mu\mathrm{m}$. Recent work on advanced CGH algorithms and intermediary optics has shown the possibility of surpassing the classical diffraction-limited resolution[38], demonstrating that holographic lithography will likely become a rich area of research for nanofabrication and beyond.

In summary, holographic grayscale lithography has enabled the single-exposure fabrication of Fabry–Perot filter arrays with tuneable cavity thicknesses and peak widths, resulting in predictable or expected optical responses. We developed a distributive simulation and fitting process that enabled us to accurately model the linewidth variation with approximated Gaussian distributions in thickness. Thus, the method consolidates the previously required multiple exposures into a single step, leverages speckle-like noise for linewidth control, and achieves a strong agreement between the experiments and TMM-based simulations, while retaining the ability to pattern features as small as 1-2.5 µm. This study demonstrated both the feasibility and potential of holographic grayscale lithography within the classical approach for scalable multispectral filter array production. Generally, it is comparable to alternative lithographic approaches; thus, it has many applications in reducing the complexity of fabrication for various uses of traditional lithography. For future research, owing to the flexibility of holograms and their control over the field of light, we anticipate that this technique will be extended to three dimensional lithography.

Conclusions

We have presented a proof-of-concept for holographic grayscale lithography of Fabry–Perot filter arrays. By leveraging SLM-based computer-generated holography, we demonstrated the single-exposure fabrication of arrays spanning cavity thicknesses of 600–1300 nm. the transmission spectra agreed strongly with transfer-matrix simulations. More importantly, we showed that speckle-like noise can be repurposed as a controllable parameter for linewidth tuning, providing a novel design strategy that surpasses conventional reflectivity-based approaches. Compared with traditional lithography, which requires multiple steps, our method demonstrates the fabrication of multiple distinct filters in a single step, significantly reducing the process complexity. The achieved resolution of 1 2.5 µm approaches the optical diffraction limit and represents a state-of-the-art technique in holographic grayscale lithography. With ongoing advances in high-frame-rate SLMs and speckle management, this approach is readily scalable to smaller pitches and enables direct integration with CMOS sensors. Our results establish holographic grayscale lithography as a promising platform for compact, reconfigurable, and mass-producible multispectral imaging devices.

Acknowledgement

O.J.B. acknowledges support from his Oppenheimer Early Career Research Fellowship. J.A.-W. acknowledges the support of his Royal Society Dorothy Hodgkin Research Fellowship. The authors also acknowledge support from the EPSRC (EP/V055003/1, EP/Z002583/1) and the ERC Proof of Concept Grant: BeyondHySpec.

Author contributions

O.J.B. and M.A. contributed to this work equally.

Data availability

The data supporting the findings of this study are available from the corresponding author upon reasonable request.

Conflict of interest

The authors declare no conflicts of interest.

References

[1] Hagen, N. A. & Kudenov, M. W. Review of snapshot spectral imaging technologies. *Optical Engineering* **52**, 090901 (Sep. 2013).

[2] Williams, C. et al. Hyperpixels: Pixel filter arrays of multivariate optical elements for optimized spectral imaging. *Light: Advanced Manufacturing* **6**, 1 (2025).

[3] Burton, O. J., Wilkinson, T. & Joyce, H. J. PCA-based polynomial transmission filter design for spectral imaging. *Optica* **13**, 119–124 (Jan. 2026).

[4] Huang, Y. et al. Multispectral imaging systems for airborne remote sensing to support agricultural production management. *International Journal of Agricultural and Biological Engineering* **3**, 50–62 (Mar. 2010).

[5] Myrick, M. L. et al. A single-element all-optical approach to chemometric prediction. *Vibrational Spectroscopy* **28**, 73–81 (Feb. 2002).

[6] Lu, G. & Fei, B. Medical hyperspectral imaging: A review. *Journal of Biomedical Optics* **19**, 010901 (Jan. 2014).

[7] Picollo, M. et al. Hyper-Spectral Imaging Technique in the Cultural Heritage Field: New Possible Scenarios. *Sensors (Basel, Switzerland)* **20**, 2843 (May 2020).

[8] Ram, B. G. et al. A systematic review of hyperspectral imaging in precision agriculture: Analysis of its current state and future prospects. *Computers and Electronics in Agriculture* **222**, 109037 (Jul. 2024).

[9] Xiang, J. et al. Ultrabroadband, High Color Purity Multispectral Color Filter Arrays. *ACS Photonics* **11**, 1163–1172 (Mar. 2024).

[10] Jia, H. et al. High-transmission polarization-dependent active plasmonic color filters. *Applied Optics* **58**, 704–711 (Jan. 2019).

[11] Wu, Z. et al. Random color filters based on an all-dielectric metasurface for compact hyperspectral imaging. *Optics Letters* **47**, 4548–4551 (Sep. 2022).

[12] Haque, S. M. et al. Design and development of Fabry–Perot etalon based color filter using ebeam GLAD technique: Simulation and experiment. *Optics Communications* **541**, 129551 (Aug. 2023).

[13] Rahman, M. A. et al. Scaling up multispectral color filters with binary lithography and reflow (BLR). *Nanophotonics* **13**, 3671–3677 (Aug. 2024).

[14] Williams, C. et al. Grayscale-to-Color: Scalable Fabrication of Custom Multispectral Filter Arrays. *ACS Photonics* **6**, 3132–3141 (Dec. 2019).

[15] Yako, M. et al. Video-rate hyperspectral camera based on a CMOS-compatible random array of Fabry–Pérot filters. *Nature Photonics* **17**, 218–223 (Mar. 2023).

[16] Goossens, T. et al. Spectral Shift Correction for Fabry-Perot Based Spectral Cameras. In 2019 10th Workshop on Hyperspectral Imaging and Signal Processing: Evolution in Remote Sensing (WHISPERS), 1–6 (2019). http://dx.doi.org/10.1109/WHISPERS.2019.8920890.

[17] Wu, R. et al. Optimized Multi-Spectral Filter Arrays for Spectral Reconstruction. *Sensors* **19**, 2905 (Jan. 2019).

[18] Sawyer, T. W. et al. Opti-MSFA: A toolbox for generalized design and optimization of multispectral filter arrays. *Optics Express* **30**, 7591–7611 (Feb. 2022).

[19] Geelen, B., Tack, N. & Lambrechts, A. A compact snapshot multispectral imager with a monolithically integrated per-pixel filter mosaic. In Advanced Fabrication Technologies for Micro/Nano Optics and Photonics VII, Vol. 8974, 80–87 (SPIE, 2014). http://dx.doi.org/10.1117/12.2037607.

[20] Yi, D. & Kong, L. Fabrication of densely patterned micro-arrayed multichannel optical filter mosaic. *Journal of Micro/Nanolithography, MEMS, and MOEMS* **10**, 033020 (Jul. 2011).

[21] Khonina, S. N., Kazanskiy, N. L. & Butt, M. A. Grayscale Lithography and a Brief Introduction to Other Widely Used Lithographic Methods: A State-of-the-Art Review. *Micromachines* **15**, 1321 (Nov. 2024).

[22] Bay, C. et al. Maskless photolithography via holographic optical projection. *Optics Letters* **35**, 2230–2232 (Jul. 2010).

[23] Fischer, D. & Sinzinger, S. Spatial Light Modulator-Based Maskless Holographic Lithography on Nonplanar Surfaces. In Imaging and Applied Optics Congress (2020), Paper HTh3H.6, HTh3H.6 (Optica Publishing Group, 2020). http://dx.doi.org/10.1364/DH.2020.HTh3H.6.

[24] Jenness, N. J. et al. A versatile diffractive maskless lithography for single-shot and serial microfabrication. *Optics Express* **18**, 11754–11762 (May 2010).

[25] Gerchberg, R. A practical algorithm for the determination of phase from image and diffraction plane pictures. *Optik* (1972).

[26] Chen, L. et al. Phase hologram optimization with bandwidth constraint strategy for speckle-free optical reconstruction. *Optics Express* **29**, 11645–11663 (Apr. 2021).

[27] Markos, P. & Soukoulis, C. M. Wave Propagation: From Electrons to Photonic Crystals and Left-Handed Materials (Princeton University Press, 2008). http://dx.doi.org/10.1515/9781400835676.

[28] Kajtár, G. et al. Theoretical model of homogeneous metal–insulator–metal perfect multi-band absorbers for the visible spectrum. *Journal of Physics D: Applied Physics* **49**, 055104 (Jan. 2016).

[29] Johnson, P. B. & Christy, R. W. Optical Constants of the Noble Metals. *Physical Review B* **6**, 4370–4379 (Dec. 1972).

[30] Tikhonov, A. N. et al. Regularization methods. In Numerical Methods for the Solution of Ill-Posed Problems (eds Tikhonov, A. N. et al.) 7–63 (Springer Netherlands, Dordrecht, 1995). http://dx.doi.org/10.1007/978-94-015-8480-7_2.

[31] Brunner, T. A. Relationship between the slope of the HD curve and the fundamental resist process contrast. *Journal of Vacuum Science & Technology B: Microelectronics and Nanometer Structures Processing, Measurement, and Phenomena* **17**, 3362–3366 (Nov. 1999).

[32] MacLeod, H. A. & Macleod, H. A. Thin-Film Optical Filters (CRC Press, Boca Raton, 2010), 4th edn. http://dx.doi.org/10.1201/9781420073034.

[33] Ali, M. N. et al. In-plane coupled Fabry–Perot microcavities based on Si-air Bragg mirrors: A theoretical and practical study. *Applied Optics* **57**, 5112–5120 (Jun. 2018).

[34] Škriniarová, J. et al. Investigation of the AZ 5214E photoresist by the laser interference, EBDW and NSOM lithographies. *Applied Surface Science* **395**, 226–231 (Feb. 2017).

[35] Andok, R. et al. The AZ 5214E Resist in EBDW Lithography and its Use as a RIE Etch–Mask in Etching Thin Ag Layers in N2 Plasma. *Journal of Electrical Engineering* **64**, 371–375 (Nov. 2013).

[36] Wang, L. et al. Speckle reduction in laser projection systems by diffractive optical elements. *Applied Optics* **37**, 1770–1775 (Apr. 1998).

[37] Lee, S. et al. Light source optimization for partially coherent holographic displays with consideration of speckle contrast, resolution, and depth of field. *Scientific Reports* **10**, 18832 (Nov. 2020).

[38] Işıl, Ç. et al. Super-resolution image display using diffractive decoders. *Science Advances* **8**, eadd3433 (Dec. 2022).